JOURNAL OF SPACECRAFT AND ROCKETS
Vol. 42, No. 3, May–June 2005

Engineering Notes

ENGINEERING NOTES are short manuscripts describing new developments or important results of a preliminary nature. These Notes should not exceed 2500 words (where a figure or table counts as 200 words). Following informal review by the Editors, they may be published within a few months of the date of receipt. Style requirements are the same as for regular contributions (see inside back cover).

Numerical Simulation of Compressible Separated Turbulent Flows over Inclined Slender Body

Xianming Liu* and Song Fu†
Tsinghua University, 100084 Beijing,
People's Republic of China

Introduction

WITH ever-increasing requirements of better performance and higher maneuverability of tactical missiles, most of the advanced tactical missiles adopt configurations with small or even without lift surfaces to reduce the zero-lift drag. When high maneuverability is required, the so-called nonlinear vortex lift generated at high angle of attack (AOA) is highly desired.

Beyond a certain AOA, primarily due to the crossflow separation of the boundary layer, vortices will appear at leeward of the slender body. The vortex sheets separate from the wall and wrap into the flow, forming a special vortex structure in space.[1–3] The behavior of the separated flow influences the aerodynamic characteristics of the slender body significantly and is, hence, the key factor that affects the lift, stability, and maneuverability of the slender body at high AOA. Deeper investigation of the flowfield around a high-AOA slender body and accurate prediction of the vortices' behavior and influences on the controllability and stability are, thus, very important to the design of tactical missiles. In fact, experimental[4–6] and numerical[7–15] investigations of the high-AOA flow about a slender body have attracted numerous researchers' attention for decades.

Because the vortex sheet from the slender body is basically the three-dimensional separation of boundary layer, it is difficult to obtain good high-AOA flow simulation results within the framework of the Euler equations (see Ref. 2). The flight Reynolds numbers are usually as high as $10^7 \sim 10^9$ for a real missile, and the flowfield is dominantly turbulent. The accuracy of Reynolds-averaged Navier–Stokes type numerical simulations depends heavily on the behavior of the turbulence model adopted. Recently, researchers have developed a number of nonlinear eddy-viscosity models to account for streamline curvature and turbulence anisotropy effects.[16–18] Nevertheless, the "simple" models with fewer requirements on computer resources are still widely employed in engineering practice.

The purpose of this Note is to assess the performance of several eddy-viscosity models in the prediction of the leeward separated flow over an ogive–cylinder at moderate high AOA when the freestream is supersonic. Detailed quantitative comparisons between numerical and experimental results will be presented for 1) surface pressure distributions, 2) the strength of the primary vortex and the location of the vortex core, and 3) normal and axial forces and pitching moment.

Governing Equations and Turbulence Models

By application of a Favre averaging technique and adoption of the Boussinesque hypothesis, the three-dimensional, compressible Navier–Stokes equations can be written in the differential form,

$$\begin{aligned}
&\frac{\partial \rho}{\partial t} + \frac{\partial \rho U_j}{\partial x_j} = 0 \\
&\frac{\partial \rho U_i}{\partial t} + \frac{\partial \rho U_j U_i}{\partial x_j} = -\frac{\partial P}{\partial x_i} + \frac{\partial \sigma_{ij}}{\partial x_j} \\
&\frac{\partial \rho E}{\partial t} + \frac{\partial \rho U_j H}{\partial x_j} = \frac{\partial}{\partial x_j}(U_i \sigma_{ij} - q_i)
\end{aligned} \tag{1}$$

Here, the stresses, heat fluxes, total energy, and enthalpy are defined, respectively, as

$$\begin{gathered}
\sigma_{ij} = (\mu + \mu_t)\left(2S_{ij} - \frac{2}{3}S_{ll}\delta_{ij}\right) - \frac{2}{3}\rho k \delta_{ij} \\
q_j = -\gamma\left(\frac{\mu}{Pr} + \frac{\mu_t}{Pr_t}\right)\frac{\partial e}{\partial x_j} \\
E = e + 0.5U_i^2 + k, \qquad H = h + 0.5U_i^2 + k
\end{gathered} \tag{2}$$

Also, $e = C_v T$, $h = C_p T$, $p = (\gamma - 1)\rho e_{,\gamma = 1.4}$, and $P_{rT} = 0.9$. The molecular viscosity μ is determined by the Sutherland law, whereas the turbulent viscosity μ_t is calculated from the turbulence model employed. Here, the Spalart–Allmaras (S–A) model,[19] Launder–Spalding (L–S) k–ε model,[20] and Shih et al. k–ε model[21] are applied.

In the S–A model, a transport equation is solved for the kinematics eddy viscosity $\tilde{v}$:

$$\begin{aligned}
\frac{\partial}{\partial t}(\rho\tilde{v}) + \frac{\partial}{\partial x_i}(\rho\tilde{v}u_i) = C_{b1}\rho\tilde{S}\tilde{v} + \frac{1}{\sigma_{\tilde{v}}}\left[\frac{\partial}{\partial x_i}\left((\mu + \rho\tilde{v})\frac{\partial\tilde{v}}{\partial x_i}\right)\right. \\
\left. + C_{b2\rho}\left(\frac{\partial\tilde{v}}{\partial x_i}\right)^2\right] - C_{w1}\rho f_w\left(\frac{\tilde{v}}{d}\right)^2
\end{aligned} \tag{3}$$

The turbulent viscosity is formulated as $\mu_t = \rho\tilde{v} f_{v1}$, and C_{b1}, C_{b2}, and $\sigma_{\tilde{v}}$ are model constants. The L–S k–ε model is a semi-empirical model based on the transport equations for the turbulence kinetic energy k and its dissipation rate ε. This model is now widely employed in solving industrial flow and heat transfer problems because of its reasonable robustness, economy, and accuracy.

The equations for k and ε are

$$\begin{aligned}
\frac{\partial}{\partial t}(\rho k) + \frac{\partial}{\partial x_i}(\rho k U_i) = \frac{\partial}{\partial x_j}\left[\left(\mu + \frac{\mu_t}{\sigma_k}\right)\frac{\partial k}{\partial x_j}\right] \\
+ P_k - \left(1 + 2M_t^2\right)\rho\varepsilon
\end{aligned} \tag{4}$$

$$\begin{aligned}
\frac{\partial}{\partial t}(\rho\varepsilon) + \frac{\partial}{\partial x_i}(\rho\varepsilon U_i) = \frac{\partial}{\partial x_j}\left[\left(\mu + \frac{\mu_t}{\sigma_s}\right)\frac{\partial\varepsilon}{\partial x_j}\right] \\
+ C_{1\varepsilon}\frac{\varepsilon}{k}P_k - C_{2\varepsilon}\rho\frac{\varepsilon^2}{k}
\end{aligned} \tag{5}$$

Received 18 April 2004; revision received 1 October 2004; accepted for publication 1 November 2004.

*Ph.D. Student, Department of Mechanics.

†Professor, Department of Mechanics. Senior Member AIAA.

The last term appearing in Eq. (4) represents the contribution of the fluctuating dilatation to the overall dissipation rate. The turbulent viscosity is defined as $\mu_t = \rho C_\mu k^2/\varepsilon$, where $C_{1\varepsilon}$, $C_{2\varepsilon}$, and C_μ are constants and σ_k and σ_ε are turbulent Prandtl numbers corresponding to k and ε, respectively. Their values are $C_{1\varepsilon} = 1.44$, $C_{2\varepsilon} = 1.92$, $C_\mu = 0.009$, $\sigma_k = 1.0$, and $\sigma_\varepsilon = 1.3$.

A desirable feature of the Shih et al. model is its satisfaction of the so-called realizable condition while keeping the relations between Reynolds stresses and strain rates linear. Realizability requires any resulting variables not to have a physically impossible value,[21] such as the negative component of turbulent kinetic energy, greater-than-one correlation coefficient, etc. In the Shih et al. model, the transport equation for k has the same form as in Eq. (4) and for ε is

$$\frac{\partial}{\partial t}(\rho\varepsilon) + \frac{\partial}{\partial x_i}(\rho\varepsilon U_i) = \frac{\partial}{\partial x_j}\left[\left(\mu + \frac{\mu_t}{\sigma_\varepsilon}\right)\frac{\partial\varepsilon}{\partial x_j}\right] + \frac{\varepsilon}{k + \sqrt{\upsilon\varepsilon}}(C_1 P_k - \rho C_2 \varepsilon) \tag{6}$$

Turbulent viscosity is different from that of the L–S k–ε model in the definition of C_μ, which is now given as $C_\mu = (A_0 + A_s U^* k/\varepsilon)^{-1}$. The model constants are $C_1 = \max[0.43, \eta/(\eta + 5)]$, $C_2 = 1.9$, $\sigma_k = 1.0$, $\sigma_\varepsilon = 1.2$, and $\eta = Sk/\varepsilon$.

The flow governing equations are spatially discretized with the finite volume method and time integrated with a five-stage Runge–Kutta method. The inviscid flux vector is evaluated with an upwind, flux-difference splitting approach.

Results

The supersonic flowfield over a 13-caliber ogive–cylinder was numerically studied. The 3-caliber ogive nose can be described as $r(x)/d = -0.002615(x/d)^3 - 0.03986(x/d)^2 + 0.30984(x/d)$. The freestream conditions are $Ma = 2.5$; AOA $= 14$ deg; $Re = 1.23e6$, based on the diameter of the aft-body (0.09398m); $P_{\text{total}} = 141{,}827$ Pa; and $T_{\text{total}} = 308$ K. Wind-tunnel tests[10,13] showed good symmetry of the flowfield; hence, only a one-half model is simulated with O-type grids. The upstream boundary of the computational domain was about three times the body length from the body nose, and the downstream was nine times the body length from the bottom. The boundary extended to three times body length in the radial direction. Nonslip, zero normal pressure gradient and adiabatic wall boundary conditions are applied to the body surfaces. For the freestream, turbulence intensity is set to 0.5%, and the turbulence viscosity is set at the same level as the viscous viscosity.

Grid sensitivity is studied on three different meshes (Table 1). The distance from the wall to the first grid point is denoted as $d1$. All grids are clustered near the slender body to provide adequate grid density to resolve the complex flow structure. The Shih et al. k–ε model is used in grid sensitivity analysis.

Table 1 Parameters of computational grids

Grid	Circumferential	Radial	Axial	$d1$
G1	70	60	91	$0.0006d$
G2	70	65	131	$0.0001d$
G3	120	75	131	$0.0001d$

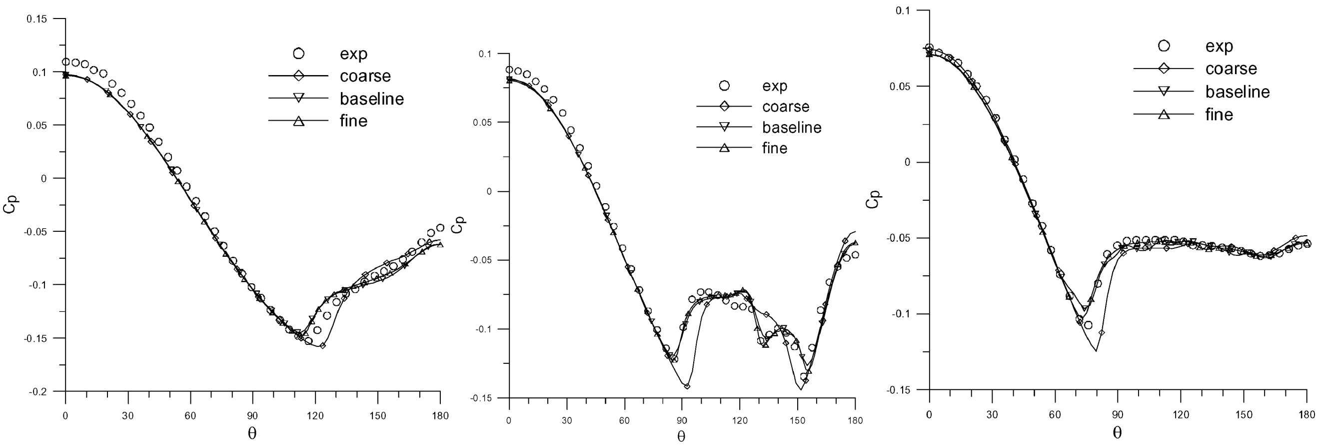

x=3.5d x=6.5d x=11.5d

Fig. 1 Surface pressure distributions for different grids.

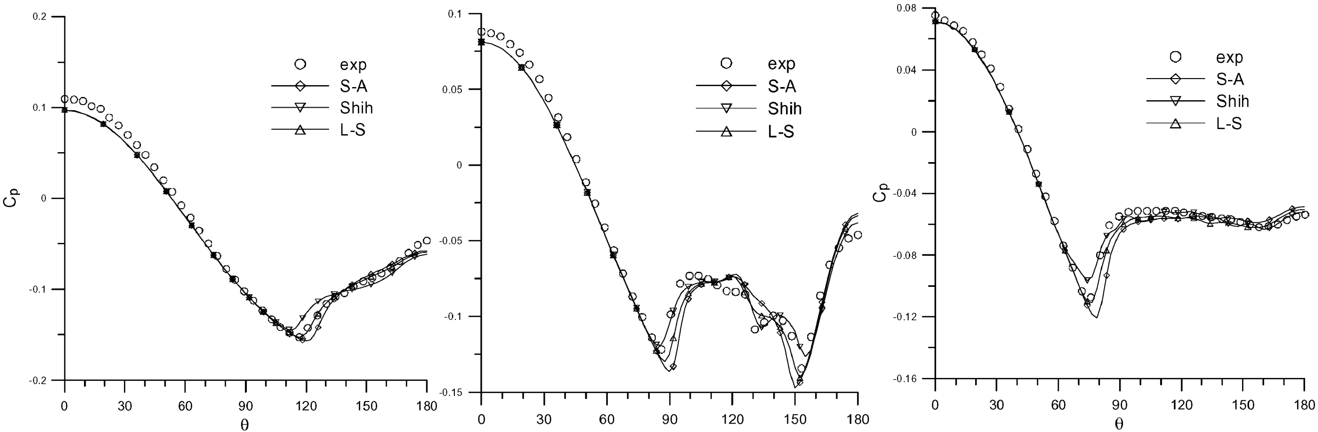

x=3.5d x=6.5d x=11.5d

Fig. 2 Surface pressure distributions for turbulence models.

The variations of the surface pressure coefficient at three cross sections ($x = 3.5d$, $6.5d$, and $11.5d$) are shown in Fig. 1. At the windward side of all three sections, computational curves of the three grids coincide with one another rather well and agree with experimental data. However, there exist noticeable differences between the results of coarser grid (G1) and the other two grids (G2 and G3) at the leeward side. At all three sections, the minimum pressures obtained by grid G1 are lower than both the experimental data and the values obtained by G2 and G3. Moreover, the azimuth angles for the minimum pressures are about 10 deg greater than those of the experimental data and the other two results. At section $x = 6.5d$, the influence of separated vortex becomes obvious and complex. The experimental pressure curve clearly shows two pressure valleys located at $\theta = 130$ and 155 deg due to the suction effect of primary and secondary vortices, respectively. The grid G1 failed to capture the valley at 130 deg, whereas the other two grids captured both valleys very well. In fact, the coarse grid result does not show a tertiary separation line. Thus, when both accuracy and efficiency are considered, the medium grid results are adopted in the discussions.

Comparisons of surface pressure distributions for the three turbulence models are shown in Fig. 2. Note that the numerical results of the three models agree with one another fairly well. At the section $x = 3.5d$, only the L–S model very accurately predicts the value and location of the minimum pressure at $\theta = 117$ deg. At the section $x = 6.5d$, all three models successfully capture the first and third pressure valleys located at 85 and 155 deg. The S–A model fails to capture the second pressure valley at $\theta = 130$ deg. Crossflow streamlines on section $x = 6.5d$ (Fig. 3) show that the S–A model gives the weakest and smallest secondary separation vortex, whereas the Shih et al. model gives the strongest and largest one. This explains why the Shih et al. model provides a better value of the pressure at $\theta = 130$ deg. At the section $11.5d$, the L–S model predicts the value and location of the minimum pressure at $\theta = 72$ deg well. From the surface streamlines shown in Fig. 4, both the L–S and Shih et al. models give better performance in resolving the tertiary separation.

The distributions of the relative total pressure, defined as the local total pressure over the value of the freestream, along a horizontal line and a vertical line across the vortex core at the section $x = 11.5d$, are shown in Fig. 5. The differences among the three models are small. Along the horizontal line (Fig. 5a), the computational curves are much steeper than the experiment. On both the left and right edges of the vortex (corresponding to $z/d \geq 0$ and ≥ 0.8, respectively), calculated relative total pressures recover to the level of unity, whereas the experimental data are less than 0.6 and 0.8. This indicates that the numerical simulations underestimate the dissipation on the horizontal edges of the primary vortex. However, Fig. 5b shows good agreement between computational and experimental results along the vertical line. Table 2 gives the geometry information, the Y and Z coordinates, of the primary vortex core at section $x = 11.5d$. From Table 2 and Fig. 5, it is shown that the numerical simulations capture the minimum total pressure and its position very well. This suggests that the strength and the core position of the primary vortex are well simulated.

Table 3 lists normal force, axial force, and pitching moment coefficients, as well as the pressure center location. Here, the reference area and length are set to the area and diameter of the cross section, respectively, and the reference point of the pitching moment is the apex of the nose. All three models obtain very good results. Compared to the experimental data, the relative errors of the normal force coefficient C_n are less than 2%. The calculated locations of

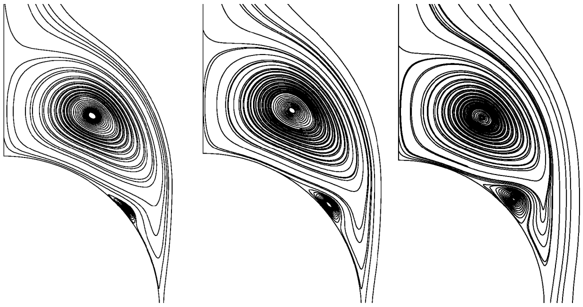

a) S–A model **b) L–S model** **c) Shih et al. model**

Fig. 3 Crossflow streamlines at section *x* = 6.5*d*.

Table 2 Vortex core coordinates at section *x* = 11.5*d*, millimeters

Coordinate	S–A	L–S	Shih et al.	Experiment
Y	88.27	88.74	87.36	90
Z	29.73	29.47	29.54	30

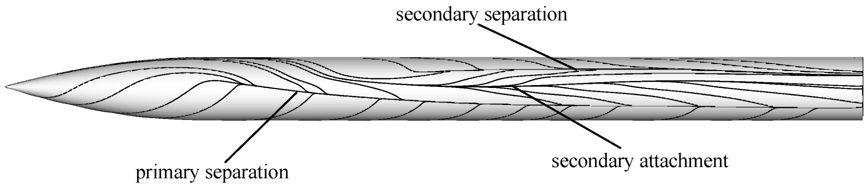

S-A model

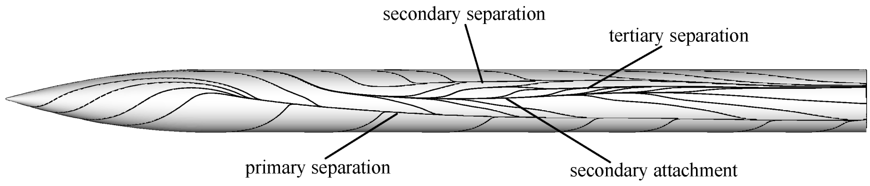

L-S model

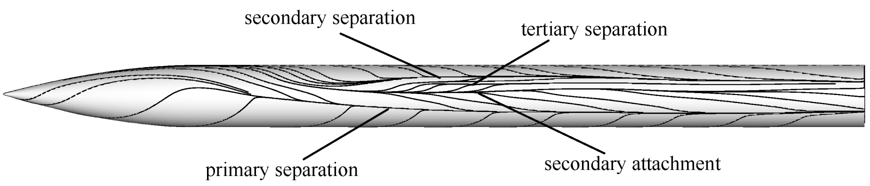

Shih model

Fig. 4 Limit streamlines on wall.

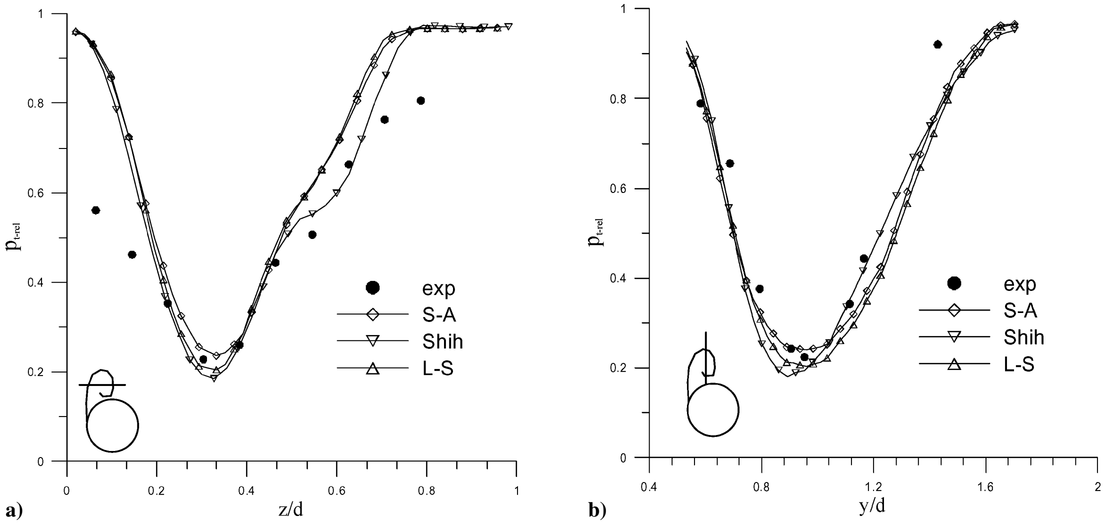

Fig. 5 Relative total pressure along lines traversing the primary vortex core at section $x = 11.5d$ along a) horizontal and b) vertical lines.

Table 3 Forces, pitching moment, and pressure center for turbulence models

Model	C_n	M_z	X_{cp}, mm	C_x	C_{xp}	C_{xv}
S–A	1.871	−10.091	506.9	0.2056	0.09824	0.10738
L–S	1.876	−10.161	509.1	0.2090	0.09892	0.11007
Shih et al.	1.874	−10.165	509.9	0.1909	0.09943	0.09148
Experiment	1.91	−10.24	504	0.1957	——	——

pressure center X_{cp} are with in 0.5% error of the whole body length. As for the axial force coefficient C_x, the largest relative error (about 6.8%) comes from the L–S model, whereas the Shih et al. model gives the lowest (2.5%). When C_x is split into two parts, that is, the pressure C_{xp} and the viscous C_{xv} components, the difference of C_x is mainly due to the difference in C_{xv}.

Conclusions

Compressible turbulent flowfields around an ogive–cylinder at moderate high AOA were numerically simulated with three eddy-viscosity models. Detailed quantitative comparisons between numerical and experimental results exhibit that all three models have satisfactorily simulated the leeward separated vortex flowfields investigated here and that the computational aerodynamic coefficients, that is, normal force, axial force, and pitching moment, and surface pressure distributions are acceptable for engineering.

Among the three turbulence models tested here, the L–S and Shih et al. models provide better details of the flowfield as can be seen from the surface pressure distributions, crossflow streamlines, and limit streamlines. The three models all underestimate the actual physical dissipation near the horizontal edges of the primary vortex at section $x = 11.5d$, causing a certain amount of discrepancies in the total pressure between experimental and computational data.

Acknowledgments

We acknowledge the support from the National Science Foundation of China (10232020), the National Key Basic Research Special Fund of China (2001CB409600), and the National High-Tech Development Program (2002AA311240).

References

[1] Champigny, P., "High Angle of Attack Aerodynamics," AGARD Special Course on Missile Aerodynamics, AGARD R-804, June 1994.

[2] Cummings, R. M., "Computational Challenges in High Angle of Attack Flow Prediction," *Progress in Aerospace Sciences*, Vol. 39, No. 5, 2003, pp. 369–384.

[3] Ericsson, L. E., "High Angle-of-Attack Aerodynamics," *Annual Review of Fluid Mechanics*, Vol. 27, 1995, pp. 45–88.

[4] Hoang, N. T., Rediniotis, O. K., and Telionis, D. P., "Hemisphere Cylinder at Incidence at Intermediate to High Reynolds Numbers," *AIAA Journal*, Vol. 37, No. 10, 1999, pp. 1240–1250.

[5] Lamout, P. J., "Pressures Around an Inclined Ogive Cylinder with Laminar, Transitional, or Turbulent Separation," *AIAA Journal*, Vol. 20, No. 11, 1982, pp. 1492–1499.

[6] Pagan, D., Molton, P., and Délery, J., "Basic Experiment on a Supersonic Vortex Flow Around a Missile Body," *Journal of Spacecraft and Rockets*, Vol. 29, No. 3, 1992, pp. 373–378.

[7] Chaderjian, N. M., "Comparison of Two Navier–Stokes Codes for Simulating High-Incidence Vortical Flow," *Journal of Aircraft*, Vol. 30, No. 3, 1993, pp. 357–364.

[8] Degani, D., and Marcus, S. W., "Thin vs Full Navier–Stokes Computation for High Angle-of-Attack Aerodynamics," *AIAA Journal*, Vol. 35, No. 3, 1997, pp. 565–567.

[9] Deniau, H., Lafon, A., and Moschetta, J. M., "Progress in the Development and Validation of a Turbulence Model for the Computation of 3D Supersonic Flows with Crossflow Separation," AIAA Paper 95-0090, Jan. 1995.

[10] Josyula, E., "Computational Simulation Improvements of Supersonic High-Angle-of-Attack Missile Flows," *Journal of Spacecraft and Rockets*, Vol. 36, No. 1, 1999, pp. 59–66.

[11] Moschetta, J. M., Lafon, A., and Deniau, H., "Numerical Investigation of Supersonic Vortical Flow About a Missile Body," *Journal of Spacecraft and Rockets*, Vol. 32, No. 5, 1995, pp. 765–770.

[12] Schiff, L. B., Degani, D., and Cummings, R. M., "Computation of Three-Dimensional Turbulent Vortical Flows on Bodies at High Incidence," *Journal of Aircraft*, Vol. 28, No. 11, 1991, pp. 689–699.

[13] Sturek, W. B., Birch, T., Lauzon, M., Housh, C., Manter, J., Josyula, E., and Soni, B., "The Application of CFD to the Prediction of Missile Body Vortices," AIAA Paper 97-0637, Jan. 1997.

[14] Morrison, J. H., Panaras, A. G., Gatski, T. B., and Georgantopoulos, G. A., "Analysis of Extensive Cross-Flow Separation Using Higher-Order RANS Closure Models," AIAA Paper 2003-3532, June 2003.

[15] Liu, X. M., and Fu, S., "Application of Several k–ε Models to the Calculation of Separated Flows on the Leeward Side of Slender Body," *Chinese Journal of Computational Mechanics*, Vol. 21, No. 4, 2004, pp. 385–391.

[16] Qian, W. Q., and Fu, S., "Curvature Sensitive Nonlinear Turbulence Model," *Acta Mechanica Sinica*, Vol. 18, No. 1, 2002, pp. 31–41.

[17] Guo, Y., and Fu, S., "On the Elimination of Wall–Topography Parameters from the Nonlinear Eddy-Viscosity Closure," *Journal of Computational Fluid Dynamics*, Vol. 10, No. 4, 2002, pp. 512–519.

[18] Fu, S., and Guo, Y., "Study of Wall-Parameter Free Low-Reynolds-Number Nonlinear Eddy-Viscosity Model," *Acta Mechanica Sinica*, Vol. 33, No. 3, 2001, pp. 145–152.

[19] Spalart, P., and Allmaras, S., "A One-Equation Turbulence Model for Aerodynamic Flows," AIAA Paper 92-0439, Jan. 1992.

[20] Launder, B. E., and Spalding, D. B., *Lectures in Mathematical Models of Turbulence*, Academic Press, London, 1972, Chap. 5.

[21] Shih, T. H., Liou, W. W., Shabbir, A., and Zhu, J., "A New k–ε Eddy Viscosity Model for High Reynolds Number Turbulent Flows—Model Development and Validation," *Computers and Fluids*, Vol. 24, No. 3, 1995, pp. 227–238.

R. Cummings
Associate Editor